

Supplemental material: Model-free measurement of the pair potential in colloidal fluids using optical microscopy

Adam Edward Stones,^{1,*} Roel P. A. Dullens,¹ and Dirk G. A. L. Aarts^{1,†}

¹*Department of Chemistry, Physical & Theoretical Chemistry Laboratory,
University of Oxford, Oxford OX1 3QZ, United Kingdom*

(Dated: August 6, 2019)

SIMULATIONS

Protocol We implemented a Grand Canonical Monte Carlo Scheme [1], in which the number of particles N is allowed to vary according to a fixed chemical potential μ .

Parameters Each simulation was carried out in a two-dimensional square box of length 50 with periodic boundary conditions. The particle-size parameter σ was set to 1 in each simulation. The configuration space was explored using three trial moves: particle insertion, particle deletion and particle movement, in the ratio 3 : 1 : 1. Initially, 10 particles were placed in the box at random and the density was allowed to increase during 10^6 equilibration steps. Subsequently, particle coordinates were taken every 10^4 moves, giving a total of 1000 snapshots. Details of the input pair potentials and parameters are given in Table SI. In all cases, the pair potential was truncated at 2.5σ , and shifted such that $u(2.5\sigma) = 0$ to maintain continuity.

EXPERIMENTS

Protocol Superparamagnetic spheres with a diameter $\sigma \approx 3 \mu\text{m}$ (Dynabeads[®] M-270 Carboxylic Acid, Invitrogen) in 20/80 % *v/v* ethanol/water were allowed to sediment in a quartz glass cell (Hellma Analytics) to form a quasi-two dimensional colloidal monolayer. The particles were magnetised by applying a magnetic field perpendicular to the sample plane using a solenoid. Samples of two different number densities were used, and measurements were taken for a range of different magnetic fields. Images were taken every second using an Olympus CKX41 bright-field microscope fitted with a $40\times$ objective and a Ximea XIQ CMOS camera. A summary of the experimental data used in the analysis is given in Table SII.

Interactions Assuming the spheres are uniformly magnetised, they behave as point magnetic dipoles from the centre of the sphere [2]. The system is quasi-two dimensional and the induced magnetic dipole moments are perpendicular to the sample plane, and so assuming that the spheres are magnetically identical, the pair potential outside of the hard core is given by

$$u(r) = \frac{\mu_0 m^2}{4\pi r^3}, \quad (\text{S1})$$

where m is the magnitude of the magnetic dipole moment on each particle and μ_0 is the magnetic constant. The relative permeability of the solvent is taken to be 1.

For sufficiently small fields, m is proportional to the magnetic flux density B and is given by $m = V_p \xi B / \mu_0$ [3], where ξ is the dimensionless volume susceptibility and $V_p = \pi \sigma^3 / 6$ is the particle volume. Substituting into (S1) and dividing by the thermal energy $k_B T$ yields

$$\frac{u(r)}{k_B T} = \frac{\alpha}{r^3}, \quad (\text{S2})$$

with

$$\alpha = \frac{\pi \sigma^6 \xi^2 B^2}{144 k_B T \mu_0}. \quad (\text{S3})$$

Field calibration A solenoid was attached to the microscope in order to apply a magnetic field perpendicular to the sample plane. We measured the resulting magnetic flux density B at the centre of the solenoid (the sample location) using a Gaussmeter (GM07, Hirst Magnetic Instruments Ltd.).

Image analysis An example of an image with the particles' positions superimposed is shown in Figure S1. The positions were measured using a customised algorithm which locates particles based on both the bright spot at the particle centre and the dark ring surrounding the particle. The images are first adjusted so that pixel intensities are spread between 0 and 1, and then each pixel is divided by the mean of all pixels within a certain radius to account for differences in the background throughout the images.

To detect the dark rings, the adjusted images are negated, and their background removed by clipping at their median pixel intensity; the images are then binarised, eroded by one pixel and their edges are detected using a Sobel filter. The outer rings are then detected using a circular Hough transform, from which the accumulators are stored. The bright spots in the accumulators correspond with the best candidates for the centres of the dark rings.

To detect the particle centres, the background of the adjusted images is removed by clipping at their median pixel intensity; the bright spots in the resulting images correspond to the centres of the particles. These images are multiplied pixel-wise by the corresponding accumulators from the Hough transform. The local maxima of

TABLE SI. The input pair potentials and parameters used in the simulation. Also shown is the mean density of each simulation.

Potential	$u(r)$	Parameters	μ	$\overline{\rho\sigma^2}$
Lennard-Jones	$4\left(\left(\frac{r}{\sigma}\right)^{12} - \left(\frac{r}{\sigma}\right)^6\right)$	$\sigma = 1$	1	0.677
Hard disk	$\infty \quad r \leq \sigma$ $0 \quad r > \sigma$	$\sigma = 1$	2	0.481
Attractive square-well	$\infty \quad r \leq \sigma$ $\epsilon \quad \sigma < r \leq \lambda\sigma$ $0 \quad r > \lambda\sigma$	$\sigma = 1$ $\lambda = 1.5$ $\epsilon = -1$	-1	0.539
Repulsive square-well	$\infty \quad r \leq \sigma$ $\epsilon \quad \sigma < r \leq \lambda\sigma$ $0 \quad r > \lambda\sigma$	$\sigma = 1$ $\lambda = 1.5$ $\epsilon = 1$	1	0.264
Attractive Yukawa	$\infty \quad r \leq \sigma$ $\left(\frac{\epsilon\sigma}{r}\right) \exp\left(-\kappa\left(\frac{r}{\sigma} - 1\right)\right) \quad r > \sigma$	$\sigma = 1$ $\kappa = 1.5$ $\epsilon = -1$	1	0.580
Repulsive Yukawa	$\infty \quad r \leq \sigma$ $\left(\frac{\epsilon\sigma}{r}\right) \exp\left(-\kappa\left(\frac{r}{\sigma} - 1\right)\right) \quad r > \sigma$	$\sigma = 1$ $\kappa = 1.5$ $\epsilon = 1$	1	0.306
Hard-core two-Yukawa (HCTY)	$\infty \quad r \leq \sigma$ $\left(\frac{\epsilon\sigma}{r}\right) \left[-\exp\left(-z\left(\frac{r}{\sigma} - 1\right)\right) + A \exp\left(-y\left(\frac{r}{\sigma} - 1\right)\right)\right] \quad r > \sigma$	$\sigma = 1$ $\epsilon = 6$ $A = 0.8$ $z = 4$ $y = 2.5$	1	0.367

these products correspond to the particles; these are then detected and their coordinates are refined using standard routines [4, 5]. Finally, spurious peaks corresponding to interstitial sites between particles are removed using distance criteria.

PAIR DISTRIBUTION FUNCTION BY TEST-PARTICLE INSERTION

Consider choosing one particle of a single-component homogenous fluid and describing all the other particles' positions relative to its centre. With this coordinate transformation, the homogeneous fluid is instead described as an inhomogeneous fluid in which all the

other particles experience an external potential due to the *source* particle which is fixed at the origin [6]. This external potential will contain a term corresponding to the pairwise interaction between the source particle and the other particles, which acts as a one-body external potential in this description, but may also contain terms corresponding to many-body interactions, which depend on the positions of multiple other particles. The number density at position \mathbf{r} relative to the source particle is given by $\rho^*(\mathbf{r}) = \rho g(\mathbf{r})$, where ρ and $g(\mathbf{r})$ are the number density and pair distribution function in the homogeneous description, in which the positions are described relative to a fixed external origin. Rearranging, we obtain

TABLE SII. Summary of the experimental data used in the analysis.

Sample	Field (mT)	Frames	$\overline{\rho\sigma^2}^a$
1	0.093	3600	0.139
1	0.142	3600	0.138
1	0.191	3600	0.143
1	0.239	2865	0.144
1	0.288	3600	0.144
1	0.386	3600	0.143
1	0.483	3600	0.110
2	0.093	3600	0.175
2	0.142	3600	0.179
2	0.191	3600	0.176
2	0.239	3600	0.177
2	0.288	3600	0.180
2	0.386	3600	0.192
2	0.483	3600	0.177

^a We used a diameter of $\sigma = 3.04 \mu\text{m}$, based on the extracted pair potentials. Note that the number density may vary within the sample due to fluctuations or changing the location of the field of view.

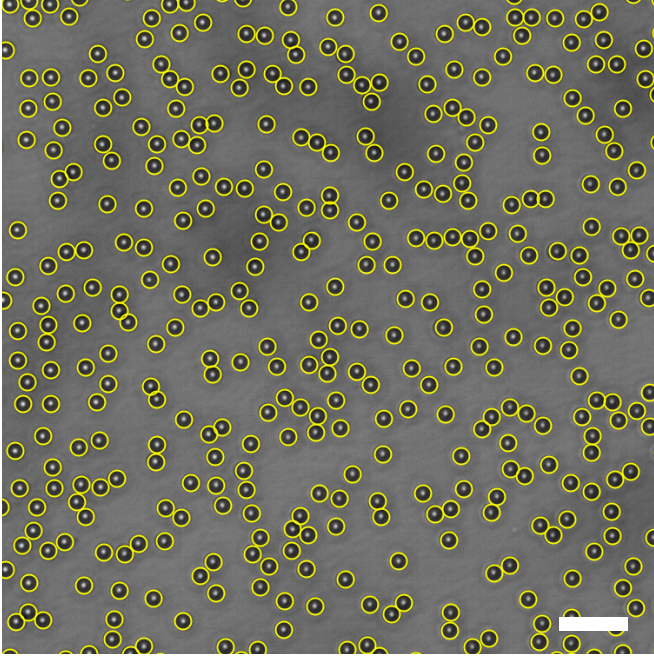


FIG. S1. Part of a typical image with particles' positions superimposed. Scale bar corresponds to $15 \mu\text{m}$. Note that the image has been adjusted so that the pixel intensities are spread between 0 and 1. Taken from Sample 2 with $B = 0.093 \text{ mT}$.

equation (1) of the main text

$$g(\mathbf{r}) = \frac{\rho^*(\mathbf{r})}{\rho}. \quad (\text{S4})$$

In the inhomogeneous description [6], $\rho^*(\mathbf{r})$ is given in the grand ensemble by

$$\rho^*(\mathbf{r}) = \frac{1}{\Xi^*} \sum_{N=1}^{\infty} \frac{z^N}{(N-1)!} \int d\mathbf{r}^{N-1} \exp(-\beta(U_N(\mathbf{r}^{N-1}, \mathbf{r}) + V_N(\mathbf{r}^{N-1}, \mathbf{r}))), \quad (\text{S5})$$

where z is the reduced activity, $\beta = (k_B T)^{-1}$ with $k_B T$ the thermal energy, U_N is the total interaction of the N particles of the fluid (which does not include the particle fixed at the origin) with one another, and V_N is their interaction with the fixed particle at the origin. The integral is over the coordinates of the first $N-1$ particles $\mathbf{r}^{N-1} \equiv \mathbf{r}_1 \cdots d\mathbf{r}_{N-1}$, and the coordinate of the N th particle \mathbf{r} is the argument of ρ^* . The grand partition function for this inhomogeneous fluid is

$$\Xi^* = \sum_{N=0}^{\infty} \frac{z^N}{N!} \int d\mathbf{r}^N \exp(-\beta(U_N(\mathbf{r}^N) + V_N(\mathbf{r}^N))). \quad (\text{S6})$$

The potential energy terms in (S5) can be split

$$U_N(\mathbf{r}^{N-1}, \mathbf{r}) + V_N(\mathbf{r}^{N-1}, \mathbf{r}) = U_{N-1}(\mathbf{r}^{N-1}) + V_{N-1}(\mathbf{r}^{N-1}) + \Psi(\mathbf{r}^{N-1}, \mathbf{r}), \quad (\text{S7})$$

where U_{N-1} and V_{N-1} are the contributions due to the first $N-1$ particles, and Ψ is the total contribution due to interactions involving the N th particle. With the substitution $M = N-1$, (S5) becomes

$$\rho^*(\mathbf{r}) = \frac{z}{\Xi^*} \sum_{M=0}^{\infty} \frac{z^M}{M!} \int d\mathbf{r}^M \exp(-\beta(U_M(\mathbf{r}^M) + V_M(\mathbf{r}^M))) \times \exp(-\beta\Psi(\mathbf{r}^M, \mathbf{r})). \quad (\text{S8})$$

Noting that M is a dummy variable, the right-hand side of (S8) is a grand ensemble average:

$$\rho^*(\mathbf{r}) = z \langle \exp(-\beta\Psi) \rangle_{\mathbf{r}}^*, \quad (\text{S9})$$

where we have dropped the subscript N . The ensemble average can be evaluated by considering Ψ to be the additional potential energy associated with hypothetical insertion of an additional particle at a position \mathbf{r} relative to an existing particle in the fluid. Note that Ψ depends on \mathbf{r} and the positions of the other particles in the fluid.

We also apply the reasoning of equations (S5) to (S9) in the homogeneous description. Setting $V_N = 0$ and dropping the star superscript yields

$$\rho(\mathbf{r}) = z \langle \exp(-\beta\Psi) \rangle_{\mathbf{r}}, \quad (\text{S10})$$

$$\rho = z \langle \exp(-\beta\Psi) \rangle, \quad (\text{S11})$$

where on the final line we have dropped the \mathbf{r} dependence since the homogeneous fluid is uniform. Noting that the reduced activity z is the same in both descriptions, we substitute (S9) and (S11) into (S4) to obtain equation (2) of the main text:

$$g(\mathbf{r}) = \frac{\langle \exp(-\beta\Psi) \rangle_{\mathbf{r}}^*}{\langle \exp(-\beta\Psi) \rangle}. \quad (\text{S12})$$

Use of this equation requires the interparticle interactions to be known; in colloidal fluids these are not known *a priori* and are measured in this work by matching g from (S12) with the result from the distance-histogram method based on (S4). In this work, the fluids are considered to be pairwise-additive and Ψ is written as a sum of pairwise interactions, which are then found using the predictor-corrector (PC) scheme in equation (3) of the main text.

In cases beyond pairwise additivity, contributions due to three-body interactions etc. can be included in Ψ and analogous PC schemes used [7] to measure them. Alternatively, the pairwise PC scheme can be used to derive *effective pair potentials* which are expected to depend on the state of the system i.e. on the density and temperature [8, 9]. Practically, this state-dependence can be used to assess the importance and nature of many-body interactions in a particular fluid. These methods will be elaborated in a forthcoming publication.

PREDICTOR-CORRECTOR SCHEME

The distance-histogram method was used to measure $g_{\text{h}}(r)$ at a range of distances r_k corresponding to the centres of the histogram intervals. The insertion result $g_j(r)$ is then calculated for the trial pair potential $u_j(r)$. Although the result can be applied directly by attempting test-particle insertion at fixed distances from the particles in the system [10], it is more efficient to attempt insertion at points on a grid over the field of view or simulation box, and approximate $\langle \exp(-\Psi/k_{\text{B}}T) \rangle_{r_k}^{(0)}$ for each r_k by averaging over points falling in the same intervals used when calculating $g_{\text{h}}(r)$. To calculate Ψ for each point, we find the distances to neighbouring particles within a cut-off radius, assuming that beyond this distance the pair potential is zero. We then use the trial pair potential $u_j(r)$ to calculate Ψ as a sum of pairwise interactions—a lookup table is used to accomplish this more efficiently. Note that the distances between the insertion points and their neighbouring particles are calculated only once, contributing to the performance of the iterative procedure.

The insertion result $g_j(r)$ is subsequently used in (3) to obtain the next correction to the pair potential, $u_{j+1}(r)$. Numerically, care must be taken when using this equation, since $g_{\text{h}}(r)$ and $g_j(r)$ for small values of r_k are often

zero, and their logarithms cannot be taken. We therefore recast the corrector (3) as

$$e_{j+1}(r) = e_j(r) \frac{g_{\text{h}}(r)}{g_j(r)}, \quad (\text{S13})$$

where $e_j(r) = \exp(-u_j(r)/k_{\text{B}}T)$. After calculating $g_j(r)$, values of zero are replaced by 10^{-20} to avoid dividing by zero. The resulting $e_{j+1}(r)$ will be zero where $g_{\text{h}}(r)$ is zero, and so these values are also replaced by 10^{-20} before the pair potential is calculated as $u_{j+1}(r) = -k_{\text{B}}T \ln e_{j+1}(r)$.

ANALYSIS

Simulation All 1000 snapshots were analysed, with 10000 insertion points used in each. The cut-off for the pair potential was 5σ , with a comparison interval of $10^{-2}\sigma$ and lookup interval of $5 \times 10^{-3}\sigma$. In each case, 250 iterations of the PC scheme were performed, and convergence was achieved.

Experiment All of the frames indicated in Table SII were used for the distance-histogram calculation, and every tenth frame was used for the insertion analysis, with 10000 insertion points in each. The cut-off for the pair potential was $34.6\mu\text{m}$, with a comparison interval of $0.138\mu\text{m}$ and lookup interval of $0.014\mu\text{m}$. Because some particles at the edges of the images were missed by the detection algorithm, we used a border cut-off of $13.8\mu\text{m}$. In each case, 500 iterations of the PC scheme were performed and the algorithm converged. Each pair potential was fit with a dipolar repulsion by recasting (S2) as

$$\ln \left(\frac{u(r)}{k_{\text{B}}T} \right) = \ln \alpha - 3 \ln r, \quad (\text{S14})$$

and fitting the data to a straight line (corresponding to the log-log plot in Figure 2) to extract α . In each case, the data between $3.94\mu\text{m}$ and $7.13\mu\text{m}$ was used, since the log-log plot shows the obtained pair potential corresponds well to a dipolar repulsion in this region.

The resulting values of α for each B were then fitted using (S3), and a value of $\xi \sim 0.9$ was extracted. Note that this value depends sensitively on the particle diameter ($\xi \propto \sigma^{-3}$); we used $\sigma = 3.04\mu\text{m}$ based on the extracted pair potentials. The temperature was estimated as $T = 298\text{ K}$.

UNCERTAINTY IN THE MEASURED PAIR POTENTIAL

Estimating the uncertainty using the noise of the measurement

Calculating the uncertainty in the measured pair potential is challenging: in principle, every iteration of the

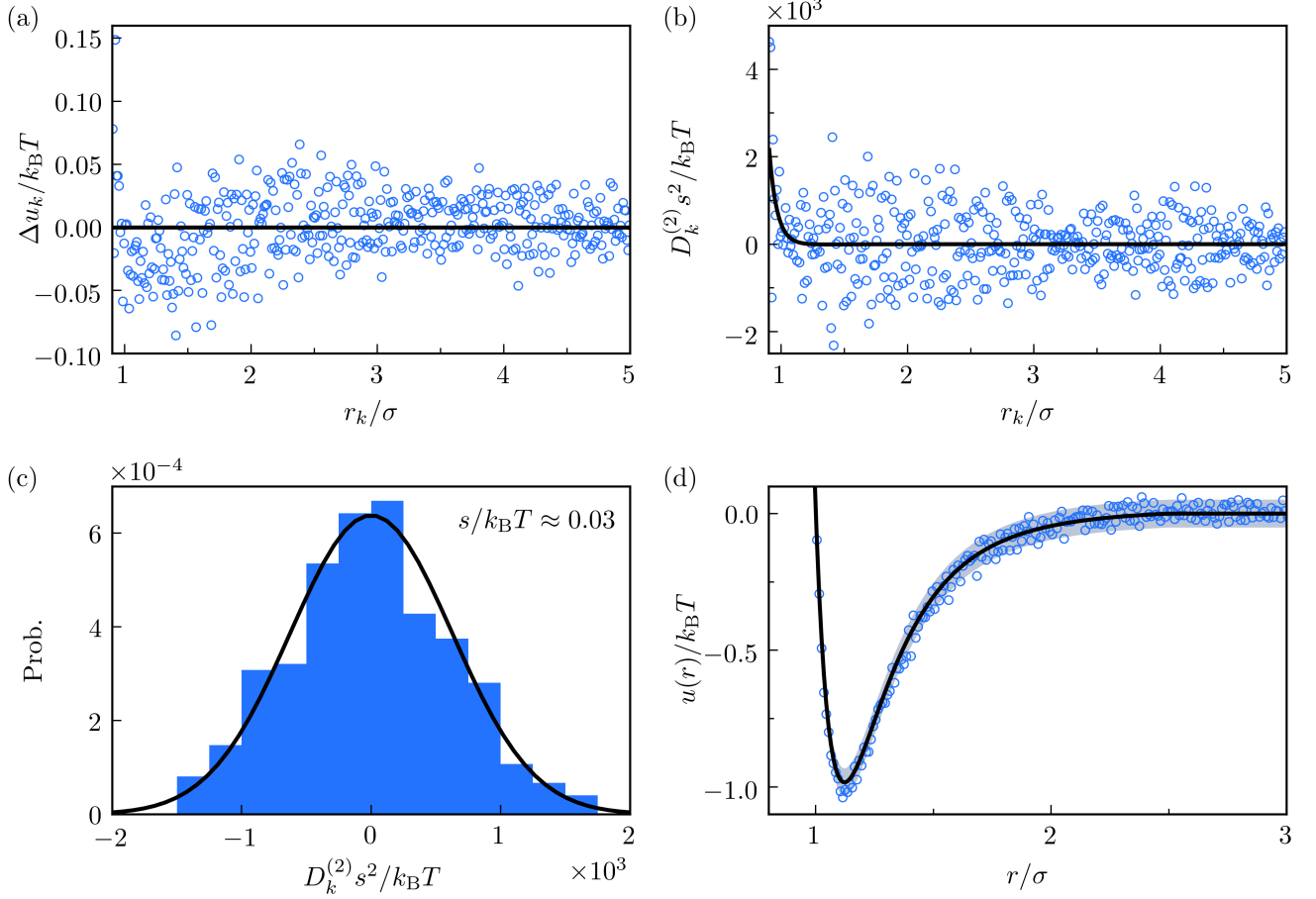


FIG. S2. (a) The deviation of the measured Lennard-Jones pair potential from the input as a function of separation. (b) The numerical second derivative of the measured pair potential (blue circles) compared with that of the true pair potential (black line). (c) A histogram of the second derivatives for separations $r_k > 2\sigma$, and the estimated normal distribution (black line). (d) Comparison of part of the measured (blue circles) and input (black line) pair potentials. The shaded area corresponds to the input pair potential $\pm 2s$.

PC scheme introduces noise from the distance-histogram and insertion measurements, but the uncertainty should stop growing after convergence. The dependence of the uncertainty on the separation r is non-trivial: for each iteration, the entire u_j is used to calculate g_j and obtain an improved pair potential, and so each separation cannot be considered independently.

In implementing the scheme, $u(r)$ is discretised and we measure a set of values u_k corresponding to the mid-points r_k of the distance-histogram bins. The deviation from the true potential \tilde{u}_k is $\Delta u_k = u_k - \tilde{u}_k$, and is assumed to be drawn from a normal distribution which is independent of separation and characterised by a standard deviation s and mean 0. We further assume that the deviations of neighbouring points are uncorrelated.

A numerical estimate of the second derivative at r_k is

given by

$$D_k^{(2)} = \frac{1}{w^2} (u_{k+1} + u_{k-1} - 2u_k), \quad (\text{S15})$$

$$D_k^{(2)} = \frac{1}{w^2} \left((\tilde{u}_{k+1} + \tilde{u}_{k-1} - 2\tilde{u}_k) - (\Delta u_{k+1} + \Delta u_{k-1} - 2\Delta u_k) \right), \quad (\text{S16})$$

where w is the bin width. Where the true pair potential is smooth, the first term on the left-hand side of (S16) is expected to be small compared with the second term and is neglected. The second term is a normally-distributed random variable with standard deviation $\sqrt{6}s/w^2$, and is used to estimate s .

Figure S2 demonstrates the application of this method in the Lennard-Jones simulation, where comparison to the exact input pair potential is possible. Figure S2(a) shows that for separations $r \geq 2\sigma$ ($u(r) \approx 0$), the deviation from the true pair potential is approximately sym-

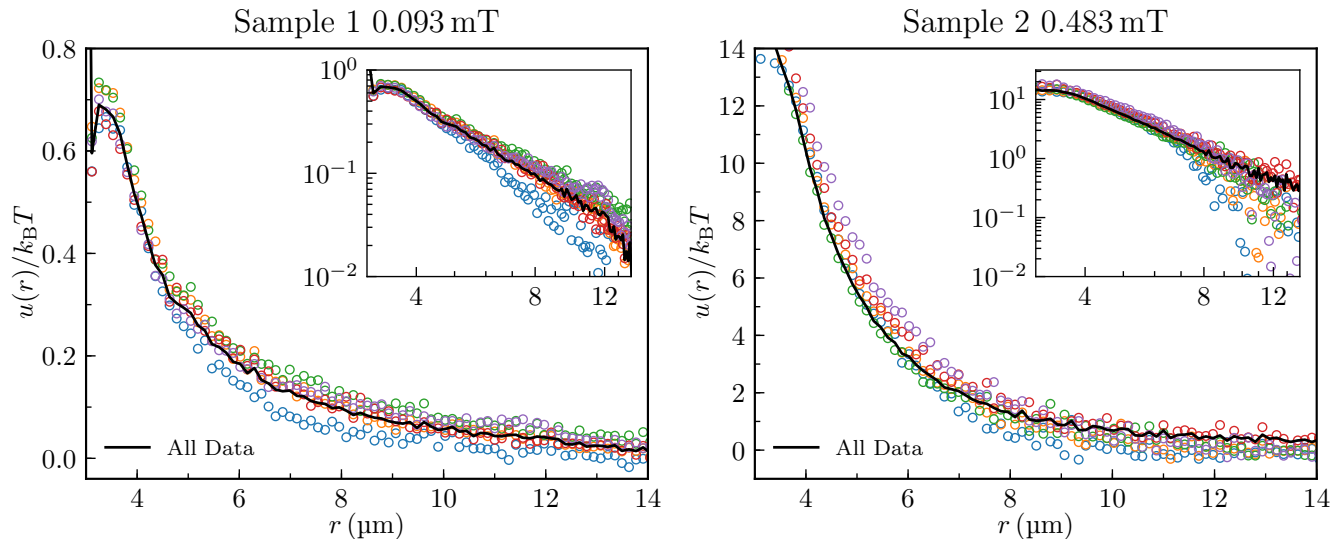


FIG. S3. Comparison of the pair potentials calculated by considering all the data (black line) with those calculated by separately considering five equal parts of the data (coloured circles). Inset: the results shown on a log-log plot.

TABLE SIII. The uncertainty in the simulation pair potentials estimated using the second-derivative method compared to that estimated directly using the input pair potential.

Pair potential	$s/10^{-2}k_B T$	
	via $D_k^{(2)}$	Direct
Lennard-Jones	2.6	2.1
Hard disk	1.0	0.8
Attractive square-well	1.6	1.3
Repulsive square-well	1.6	1.3
Attractive Yukawa	1.5	1.6
Repulsive Yukawa	1.2	1.3
Hard-core two-Yukawa (HCTY)	1.0	0.8

metric about 0. Figure S2(b) confirms that the second derivative of the true pair potential makes a negligible contribution to the second derivative of the measured pair potential $D_k^{(2)}$ at these separations. The corresponding $D_k^{(2)}$ are shown in Figure S2(c) to obey the anticipated normal distribution, with $s \approx 0.03k_B T$. In Figure S2(d), we compare the measured $u(r)$ to the true $u(r)$ and find the deviations to be well-captured by a spread of $\pm 2s$. In Table SIII, we compare the estimates of s for each simulation to those obtained by considering the deviation from the true pair potentials, finding good agreement in all cases.

For each of the experimentally-measured pair potentials, we considered separations larger than $5 \mu\text{m}$ and obtained a normal distribution analogous to that of Figure S2(c). We show the extracted uncertainties in Table SIV;

TABLE SIV. Estimates of the uncertainties in the experimental measured pair potentials.

Field (mT)	$s/10^{-2}k_B T$	
	Sample 1	Sample 2
0.093	0.4	0.3
0.142	0.5	0.4
0.191	0.5	0.6
0.239	0.7	0.7
0.288	0.8	1.2
0.386	1.2	3.0
0.483	2.0	6.7

$s < 0.1k_B T$ in all cases, corresponding to the good power-law fits in Figure 2 of the main text.

Sensitivity of the measurement to the input

We also investigated the sensitivity of the method to the input data. Using fewer configurations, i.e. shorter simulations or experiments, gives rise to more noise in $g_h(r)$ and the $g_j(r)$ obtained when implementing the PC scheme. This leads to more noise in the measured pair potential and can result in the PC scheme failing to converge. To investigate the effect of limited data, we reanalysed the two samples corresponding to the least (Sample 1, 0.093 mT) and greatest (Sample 2, 0.483 mT) structure. The data was split into five consecutive parts of equal length, and each part analysed separately.

The measured pair potentials are shown in Figure S3. In all cases, the qualitative repulsive behaviour is captured, though the finer quantitative details are lacking, particularly at large separations. We stress that there is considerable advantage in using all of the data simultaneously in the inversion, rather than splitting the data in this way and calculating the average result. In principle, more data can be obtained by performing longer experiments or simulations.

DATA AND CODE AVAILABILITY

The data and code used in this letter are available from the corresponding authors on request. All figures have associated raw data.

-
- * adam.stones@chem.ox.ac.uk
† dirk.aarts@chem.ox.ac.uk
- [1] D. Frenkel and B. Smit, *Understanding Molecular Simulation: From Algorithms to Applications (Computational Science Series, Vol 1)* (Academic Press, 2001).
 - [2] B. F. Edwards, D. M. Riffe, J.-Y. Ji, and W. A. Booth, *Am. J. Phys.* **85**, 130 (2017).
 - [3] J. Ge, L. He, Y. Hu, and Y. Yin, *Nanoscale* **3**, 177 (2011).
 - [4] J. C. Crocker and D. G. Grier, *J. Colloid Interface Sci.* **179**, 298 (1996).
 - [5] D. Allan, T. Caswell, N. Keim, and C. van der Wel, “trackpy: Trackpy v0.3.0,” (2015).
 - [6] J.-P. Hansen and I. R. McDonald, *Theory of Simple Liquids, Fourth Edition: with Applications to Soft Matter* (Academic Press, 2013).
 - [7] C. Ruß, M. Brunner, C. Bechinger, and H. H. von Grünberg, *EPL* **69**, 468 (2005).
 - [8] J. A. Barker, D. Henderson, and W. R. Smith, *Mol. Phys.* **17**, 579 (1969).
 - [9] A. A. Louis, *J. Phys. Condens. Matter* **14**, 9187 (2002).
 - [10] A. E. Stones, R. P. A. Dullens, and D. G. A. L. Aarts, *J. Chem. Phys.* **148**, 241102 (2018).